# VISIONS - VISTA Star Formation Atlas
# Data Release 2

Programme ID: **198.C-2009**
Authors: S. Meingast, J. Alves, H. Bouy for the VISIONS collaboration

## Abstract

VISIONS is a near-infrared (NIR) VISTA public survey covering all major nearby star-forming regions accessible from the southern hemisphere. The survey is designed to deliver *deep* high-sensitivity observations of areas with large amounts of extinction, *control* fields which sample the predominant stellar populations in largely extinction-free regions, and *wide* field data in multiple epochs on large areas surrounding the targeted star-forming regions. This data release contains all collected observations from April 2017 to October 2021 on the Corona Australis star-forming region for a total of 3360 submitted files. The area covered amounts to about 43 deg$^2$. The release comprises contiguous tiles, as well as stacked pawprints, corresponding weight maps, and source tables. All data were processed with a newly implemented pipeline environment operated at the University of Vienna that will also be used for subsequent data releases. Astrometric calibration was performed with respect to Gaia EDR3, resulting in a typical dispersion of about 15-20 mas. Photometric calibration relies on a direct comparison to 2MASS with statistical and systematic uncertainties at the percent level or better for bright sources. The image quality is excellent throughout the entire survey with most data featuring point source FWHMs better than 1 arcsec. Compared to 2MASS, the survey reaches up to 6 mag fainter sensitivity limits.

## Release content

### Overview of Observations

The VISIONS public survey is split into three distinct sub-surveys: *deep*, *control*, and *wide*. The *deep* fields deliver high-sensitivity data on the regions with the largest amount of extinction. The *control* fields were designed to reach a similar photometric sensitivity as the *deep* fields, but target regions with low amounts of extinction. The *wide* fields monitor a large region to enable the computation of proper motions for sources inaccessible to Gaia. This data release contains all VISIONS observations on the Corona Australis star-forming region. In total, 160 tiles have been observed between April 2017 and October 2021. Figure 1 displays an overview of

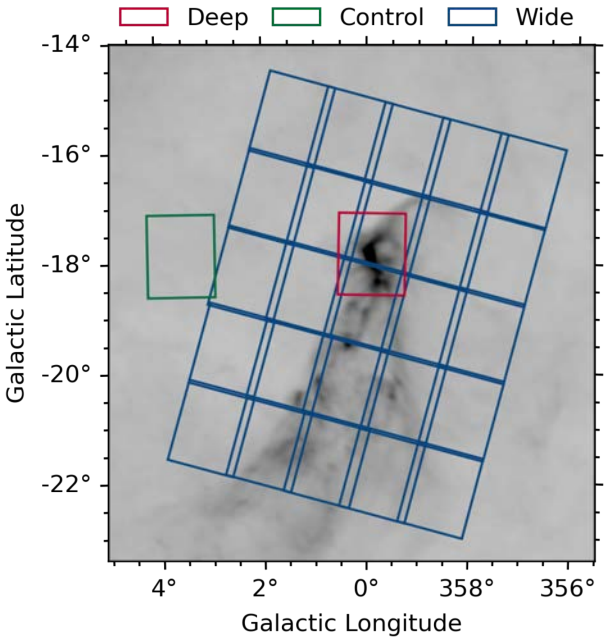


**Fig. 1.** Coverage of VISIONS for the Corona Australis star-forming region displayed on top of a Planck 857 GHz image. Individual boxes represent full VIRCAM tiles.

the targeted areas of the individual sub-surveys on top of a Planck image in the 857 GHz band. Figure 2 marks the observing times for all collected data. Figure 3 displays source densities on several healpix maps for all data products. Clearly visible are the outline of the molecular cloud and the globular cluster NGC 6723 in the northern portion of the *deep* field. The *wide* fields exhibit a particular pattern that is produced by different observing conditions. In the following paragraphs, we list properties for *deep*, *control*, and *wide* data.

***Deep***

There are in total 6 deep tiles included in this data release. All observations are centered approximately on l=359.893 deg, b=-17.851 deg, target the region with the largest amount of extinction toward the Coronet cluster, and cover an area of about 1.2 x 1.5 $deg^2$. This field is displayed in red in Fig. 1. Furthermore, the *deep* fields were observed twice in each NIR filter J, H, and Ks in order to keep the total OB runtime below 1 hour. J band data were imaged with DIT = 3s, NDIT = 10, and NJITTER = 3, the H and Ks bands were observed with DIT = 2s, NDIT = 25, NJITTER = 3. In addition, an offset field was sampled during the observations to construct a more reliable background model. The total effective exposure time amounts to 300 s for one tile, or 600 s for both deep sequences in each passband. The *deep* data were collected in April 2018, marked in red at the top of Fig. 2.

***Control***

To sample the unextincted galactic field population, the VISIONS survey includes a region about 4 degrees to the (galactic) east of the *deep* field at the same galactic latitude (displayed in green in Fig. 1). The field is centered on l=3.556 deg, b=-17.865 deg with an area of 1.2 x 1.5 $deg^2$ and was observed once in each J, H, and Ks passband. The observing setup was DIT= 5 s, NDIT = 10, NJITTER = 6 for J, and DIT= 2 s, NDIT = 25, NJITTER = 6 for H and Ks. The effective exposure times of the resulting tiles are 600 s. Since no extended emission is present in this field, sky offsets were not included for these observations. The *control* data were collected in May (J and H) and July (Ks) 2018, as marked with a green bar at the top of Fig. 2.

***Wide***

The wide field survey covers large parts of the Corona Australis molecular cloud and spans a region of about 5.6 x 7.3 $deg^2$. This area was observed in 6 different epochs – named A through F – where each epoch consists of a contiguous field of 25 tiles arranged in a 5x5 pattern. These observations were exclusively conducted in the H passband and are displayed in blue in Fig. 1. All *wide* data were taken with DIT = 3 s, NDIT = 2, NJITTER = 5 without sky offsets, resulting in an effective exposure time of 60 s per tile. The *wide* data were mainly taken from April 2017 (ESO period 99) to September 2019 (ESO period 102). A set of four tiles in epoch E was not observed during their scheduled period; these were collected in March 2021. In addition, the wide survey contains an additional epoch for the *deep* field region at the end of the survey timeframe in October 2021, named *deep WX* (wide epoch X). Considering only VISIONS data, the *WX* epoch extends the baseline for proper motion calculations in the *deep* field region from about 3 years to 4.5 years.

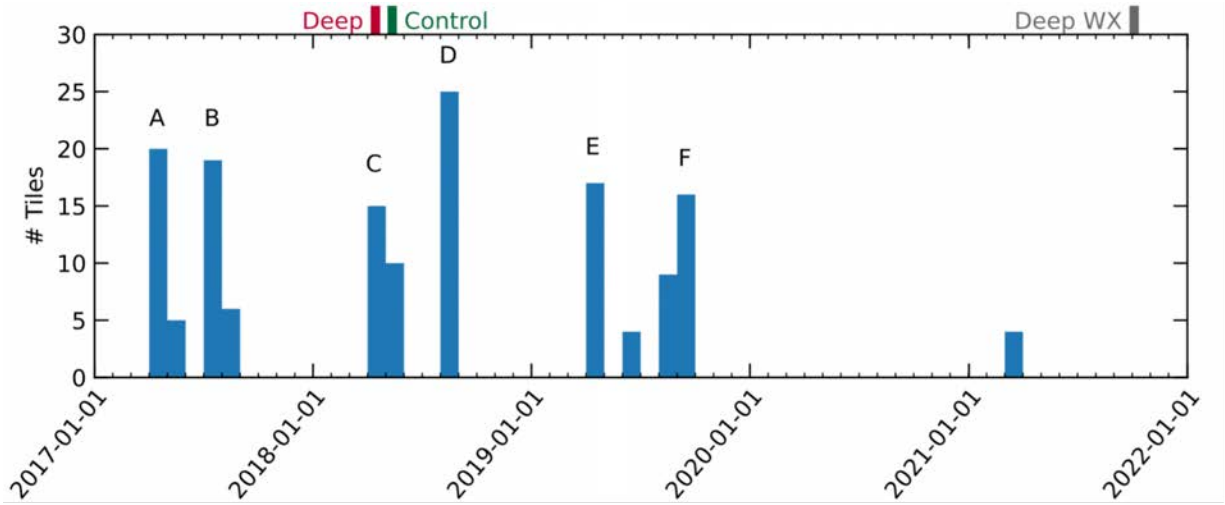


**Fig. 2.** Observing dates for all data included in this release. *Wide* field data are displayed as a blue histogram. Observing times for the *deep*, *control*, as wells as the additional *deep WX* epoch are marked at the top in red, green, and grey, respectively. The four tiles observed in March 2021 are part of epoch E.

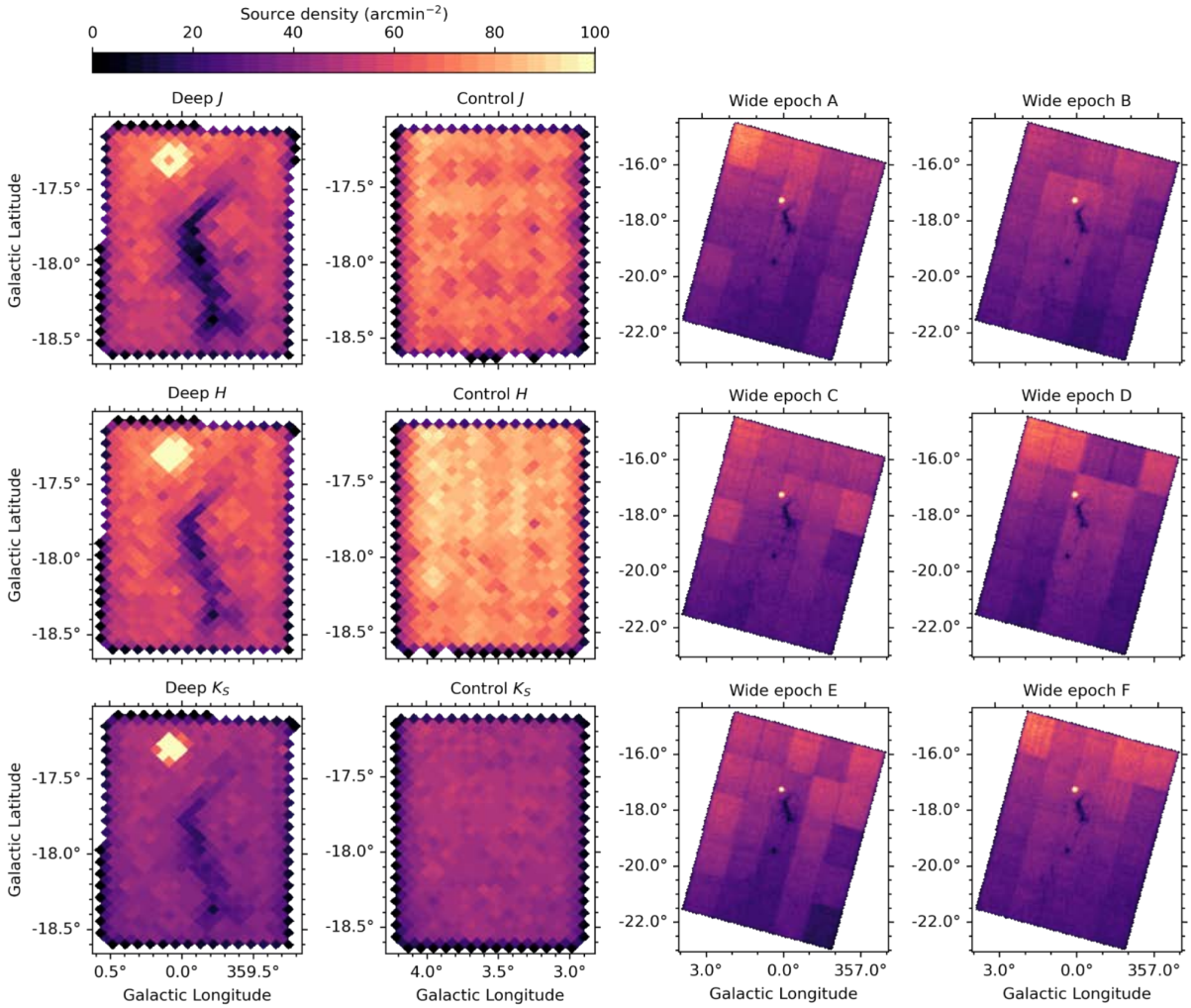


**Fig. 3.** Number of sources per arcmin$^2$ on a healpix grid (nside = 1024, pixel area ~ 11.8 arcmin$^2$). Clearly, the outline of the molecular cloud becomes visible in the *deep* and *wide* fields. The prominent overdensity in the deep fields is the globular cluster NGC 6723. Also, a pattern for the wide fields is visible as a result from the different sensitivity due to variable observing conditions.

## Data Volume

In total 4800 pawprints were requested for the Corona Australis region in the VISIONS program. Out of these, only a few frames were not usable, mostly due to distorted PSF shapes likely resulting from telescope tracking issues. Pawprints affected by such issues were manually removed since the pipeline raises an error when irregular PSF shapes are detected. After removing problematic observations, the submitted Phase 3 data were constructed from 4791 raw input pawprints where 4521 belong to the wide survey (including the extra *deep WX* epoch), 162 to the *deep* survey (including sky offsets), and 108 to the *control* survey. From this input, we constructed a total number of 3360 phase 3 files amounting to about 840 GB in data volume. Image data submitted to the phase 3 archive includes, for each observed field, photometrically and astrometrically calibrated tiles and stacked pawprints. For each of these image products, a corresponding source table is also provided.

# Release Notes

In this section, we briefly describe the individual data processing steps, followed by an analysis on the data quality and photometric and astrometric properties. Further, we describe the format of the submitted data and give a description of the content of the source catalogs.

## Data processing

Data processing closely follows the series of steps outlined in Meingast et al. 2016, but implements a series of improvements and additions across all processing modules. Here, we only briefly describe the steps, as the full procedures will be described in detail in an upcoming manuscript dedicated to this topic. Calibration files are directly fetched from the ESO science archive through the association in the Download Portal.

Initially, all provided calibration data are grouped into their respective categories from which main calibration data products are constructed. This includes bad pixel masks, tables holding coefficients to correct for detector non-linearity, dark current information, gain and read-noise tables, flat fields, and global weightmaps for optimal source detection. The procedures in this module deliver a main calibration library that contains all the above-listed products and a series of quality control measures. As an example, Fig. 4 shows a non-linearity correction for the detectors 3 and 4. All products constructed at this stage serve as input for processing the actual science data.

Independent from the production pipeline of the main calibration files, the raw science data pass through a sequence of dedicated processing steps. In a first step the input data are linearized followed by subtracting the dark current (for the specific given DIT and NDIT combination) and normalizing the data with the corresponding flat field. At this step, also the image headers are purged, only retaining the most important entries and the (uncalibrated) astrometric solution is standardized. The latter step is necessary since oftentimes the ESO data flow system does not produce reliable WCS parameters in the headers for VIRCAM.

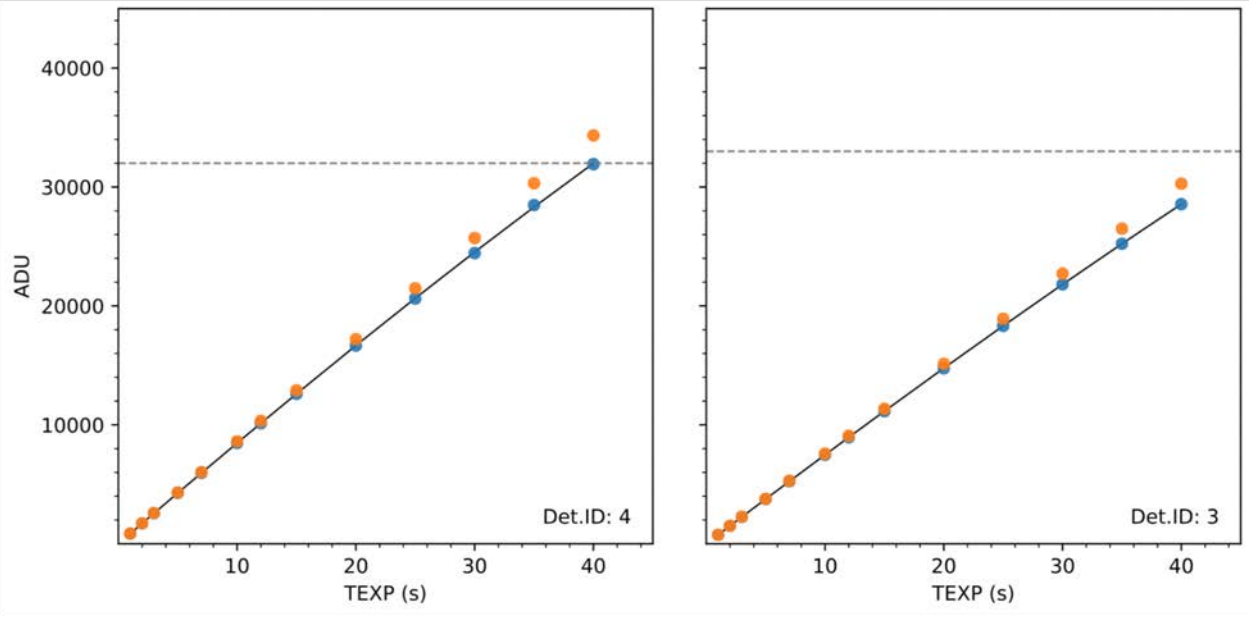


**Fig. 4.** Measured flux in ADU as a function of exposure time in seconds for the VIRCAM detectors 3 and 4 to determine the non-linearity correction. The blue dots depict the measured input flux, the orange dots the linearized values. The solid black line is a polynomial fit that is used for the inversion. The horizontal dashed line represents the approximate saturation levels.

Following the basic processing stage, the pipeline creates several additional data products that are specific to the given input observations. This includes photometric (2MASS) and astrometric (Gaia EDR3) reference tables, source masks, and a background model. Subsequently, the background model is applied to the data that already ran through the basic calibration. At this step also cosmetic corrections are applied where a characteristic striped pattern is removed from the images as well as some bad pixels are interpolated. Also, the previously built source masks are applied to the data to perform an additional smoothed correction of residual patterns in the background.

After the advanced processing stage, the pipeline performs the astrometric calibration. Here, we first generate the astrometric projection of the final tile where we chose a zenithal equal area projection (WCS code ZEA) with a pixel scale of ⅓ arcsec/pix. The rotation of the output tile is optimized so that the footprint in pixel size is minimized. Subsequently, we perform an initial source extraction with Sextractor, specifically set up to provide the necessary data for the astrometric calibration with the Scamp package. We chose a fourth-order polynomial to map the distortion pattern of the instrument and use positions from Gaia EDR3 as reference. Despite Gaia being an optical survey, no issues were found even in highly extincted areas.

Instead of calibrating the data to the Gaia EDR3 epoch (J2016.0), we chose to perform a more precise calibration where we warp the source positions in the Gaia catalog to the observing time of the given observing sequence. In this way, the data are astrometrically calibrated to their actual observing time, instead of relying on a mean epoch for all sources. However, for most purposes, assuming a global mean epoch of 2018.5 will be sufficient. The computed astrometric solution is then saved to external headers. Figure 5 shows a typical quality control

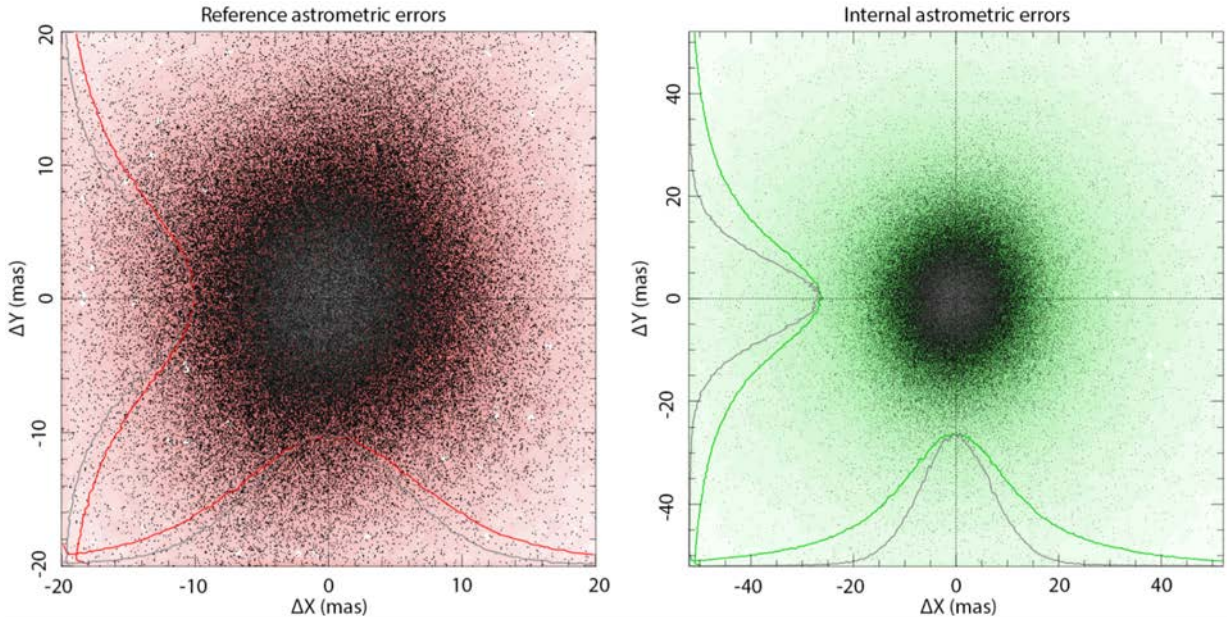


**Fig. 5.** Astrometric errors for a typical batch of processed files as derived by Scamp. The left plot shows the astrometric errors with respect to Gaia EDR3. The plot on the right-hand side shows the internal astrometric errors, i.e. the rms in internally cross-matched positions (each source is imaged several times, depending on the number of offset and jitter positions). The colored lines on the left y axis and bottom x axis show histograms that refer to all input sources and a subset with high S/N, respectively.

plot produced by Scamp. While the panel on the left shows astrometric errors with respect to the reference catalog, the right panel displays the internal errors, i.e. comparing detected source positions as found in the VISIONS images.

Following the astrometric calibration, the pipeline constructs an illumination correction by comparing the measured source fluxes to 2MASS. For a clean subsample of sources in the observed data, the pipeline cross-matches the sources with the photometric reference catalog and computes zero-point offsets. Moreover, at this stage also all data are scaled to have a common zero-point of 25 mag. We chose to scale all images to a fixed zero-point since this step later facilitates a more reliable co-addition for images observed under different observing conditions. The scaled zero-points are computed on a spatially variable map with an adaptive kernel size (depending on the number of available sources). The resulting illumination correction is immediately applied to the data and contains information on residual offsets that were not corrected during flat-fielding. Figure 6 displays an example of an illumination correction for the detectors 1 and 2. Comparing these detectors, the plot already shows a deviation of a few percent as a result of imperfect flat-fielding.

The next step in the calibration procedure applies the astrometric solution to the processed, illumination-corrected images and resamples all data onto the previously-defined common projection. To this end, we use the Swarp package. From these scaled and resampled pawprints, the final image data products are produced. These are stacked pawprints, i.e. combined individual offset positions (the combined jitter pattern) and fully contiguous tiles. We then performed source extraction on these images with Sextractor with a detection threshold of 1.5 sigma where we require a source to consist of at least 3 significant pixels. For the resulting source tables, the pipeline computes a global zero-point for each separate

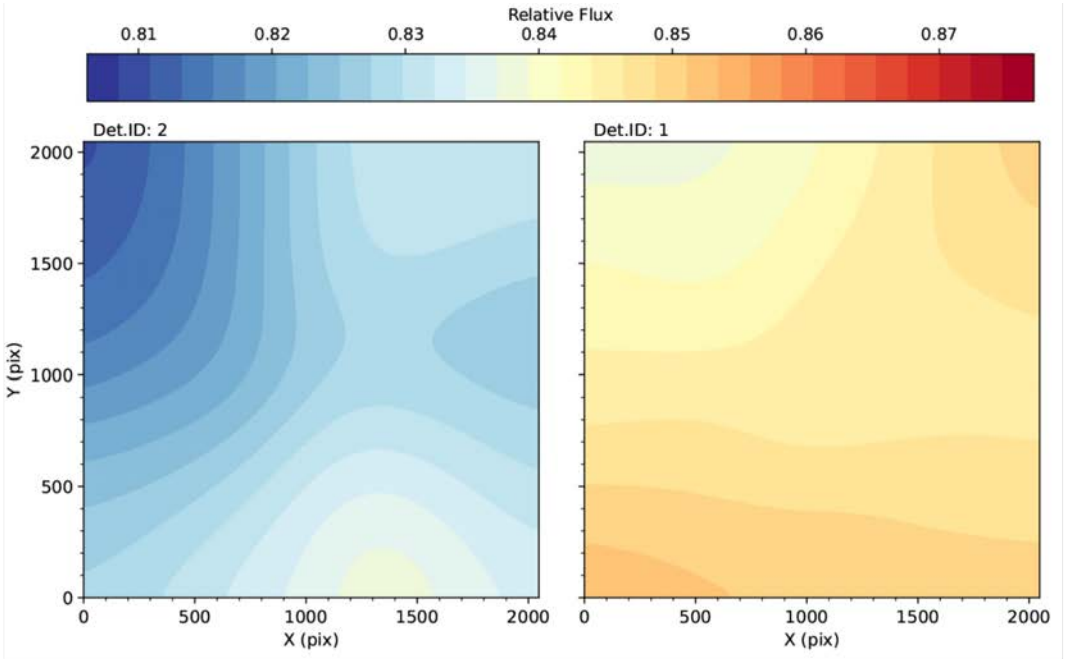


**Fig. 6.** Example of the illumination correction for the VIRCAM detectors 1 (right panel) and 2 (left panel). During data processing, all images are furthermore normalized to a zero-point of 25 mag.

image data unit, i.e. the full tile, or the individual detectors in case of the stacked pawprints. The zero-point is once again derived with a comparison to 2MASS sources. Here, we find that the final zero-point deviates slightly (a few percent at most) from the initial value of 25 mag due to the intermediate resampling step. Applying this zero-point to the measured fluxes then yields the final photometric values included in this data release.

Finally, we note here that the above-outlined procedure is only a coarse description of the underlying algorithms. In fact, each step depends on a series of parameters and specific setups that were carefully assessed in a long series of tests prior to the application of the pipeline to the VISIONS raw data. A comprehensive description of the full procedures with details on all individual components will be part of an upcoming publication. We also note that the source code for the pipeline is currently not publicly available, but will be made open source upon the final VISIONS data release at the latest.

## Data Quality

In this section we review the general data quality, including statistics on source ellipticities and FWHM and assess the photometric and astrometric performance. In order to derive robust statistics and to only retrieve reliably measured point sources, we applied a series of quality criteria to the full input catalogs prior to computing the statistics. These are:

- ➔ S/N > 50 (as measured by Sextractor)
- ➔ 12 mag < source magnitude < 16 mag (remove saturated sources and most galaxies)
- ➔ Sextractor flags < 4 (allowing deblending of sources)
- ➔ 1.2 pix < FWHM < 5 pix (0.4 < FWHM < 1.66 arcsec)

## Properties of point sources

To assess the image quality across all observed regions, we analyzed the measured FWHM and ellipticity for all point sources in the data release. Figure 7 shows cumulative histograms for source ellipticities across all VISIONS sub-surveys. The left-most panel displays data for the *deep* observations, *control* data is displayed in the center, and the histogram on the right-hand side shows the ellipticity for sources in the *wide* fields. The panel for the *wide* observations shows individual epochs as light green histograms. The dark green line depicts concatenated data for all *wide* fields. Since the source ellipticity varies only marginally, the individual epochs are barely visible in the panel on the right. Across all surveys we observe excellent image properties, where about 80% of all (point-like) sources feature ellipticities < 0.1. Figure 8 shows the same ellipticity statistics, but mapped onto a healpix grid for all data products (nside = 1024, pixel area ~ 11.8 arcmin$^2$). The figure reveals a pattern where especially the *wide* field data show variable degrees of ellipticity across the entire field. A closer inspection of the panels describing the *wide* fields reveals a checkerboard pattern for some tiles. For these tiles, the observing condition varied during the execution of an OB. This change, however, was not large enough to warrant a repetition of the affected observations. Furthermore, the globular cluster NGC 6723 becomes visible in this visualization due to difficulties with de-blending sources in this region.

Following the layout of Figs. 7 and 8, the plots in Figs. 9 and 10 show the image quality parametrized with the point source FWHM. We find that well above 80% of all observations were carried out in excellent atmospheric conditions with FWHM values below 1 arcsec. For the *deep* fields more than 50% of the data reaches an image quality of < 0.7 arcsec. Among the *control* fields, the H band was observed under the best conditions. Figure 10 maps the measured point source FWHM onto a healpix grid (nside = 1024, pixel area ~ 11.8 arcmin$^2$). This view reveals variations of the image quality on both large and small scales. Since the observations for the *wide* fields within an epoch were carried out over the course of multiple weeks, the image quality can greatly vary between adjacent fields. For example, in epoch D, two tiles to the (galactic) North were imaged with a point source FWHM around 1 arcsec, while the immediately surrounding tiles feature much better observing conditions. Furthermore, we oftentimes find a characteristic checkerboard pattern across individual tiles. This pattern is a consequence of the typical observing pattern with VIRCAM and – similar to the ellipticity maps – shows that observing conditions varied during the execution of individual OBs. Regarding the *wide* data, we observe a large spread in image quality with epoch D featuring the best values while the data for epoch B was collected mostly under worse (but still excellent) conditions. Moreover, the Fig. 9 shows that many sources were imaged under such excellent conditions that the resulting PSFs are undersampled. For a pixel scale (prior to resampling) of ⅓ arcsec/pix and a regular observing pattern, ideally FWHMs values should never be far below ⅔ arcsec. For the *deep* data we find that this is the case for about 25% of all sources in J and Ks and 80% for the H band. About 50% of all sources in the H band control data exceed this limit. The values for wide epochs A through F are 3%, 1%, 23%, 40%, 31%, and 15%, respectively.

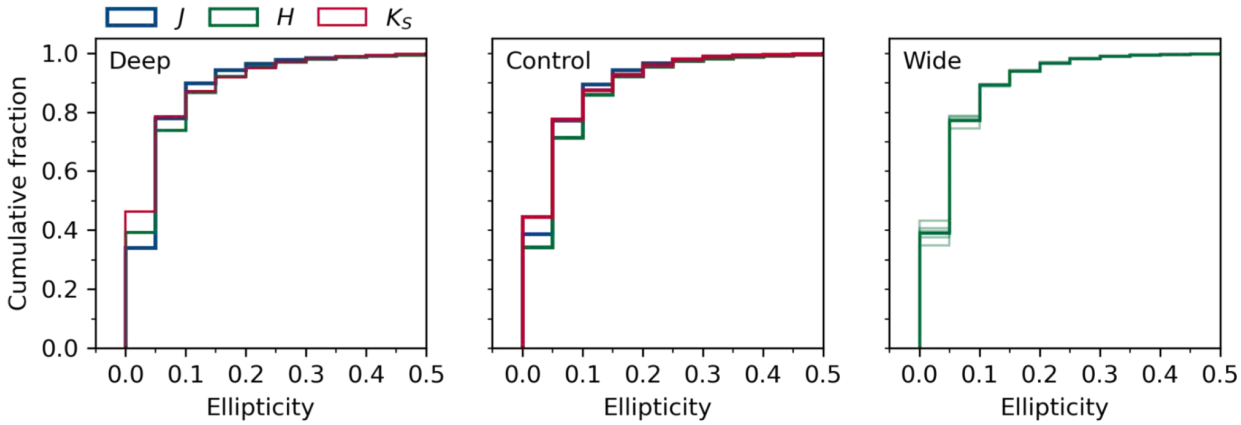


**Fig. 7.** Cumulative histograms for the measured ellipticity of point sources across all VISIONS surveys. The panels from left to right represent *deep*, *control*, and *wide* data, respectively. The rightmost panel also displays histograms for individual epochs in light green; these, however, are only marginally visible due to their similarity. The dark green line combines all wide field data. Different histogram colors represent the NIR passbands J (blue), H (green), and Ks (red).

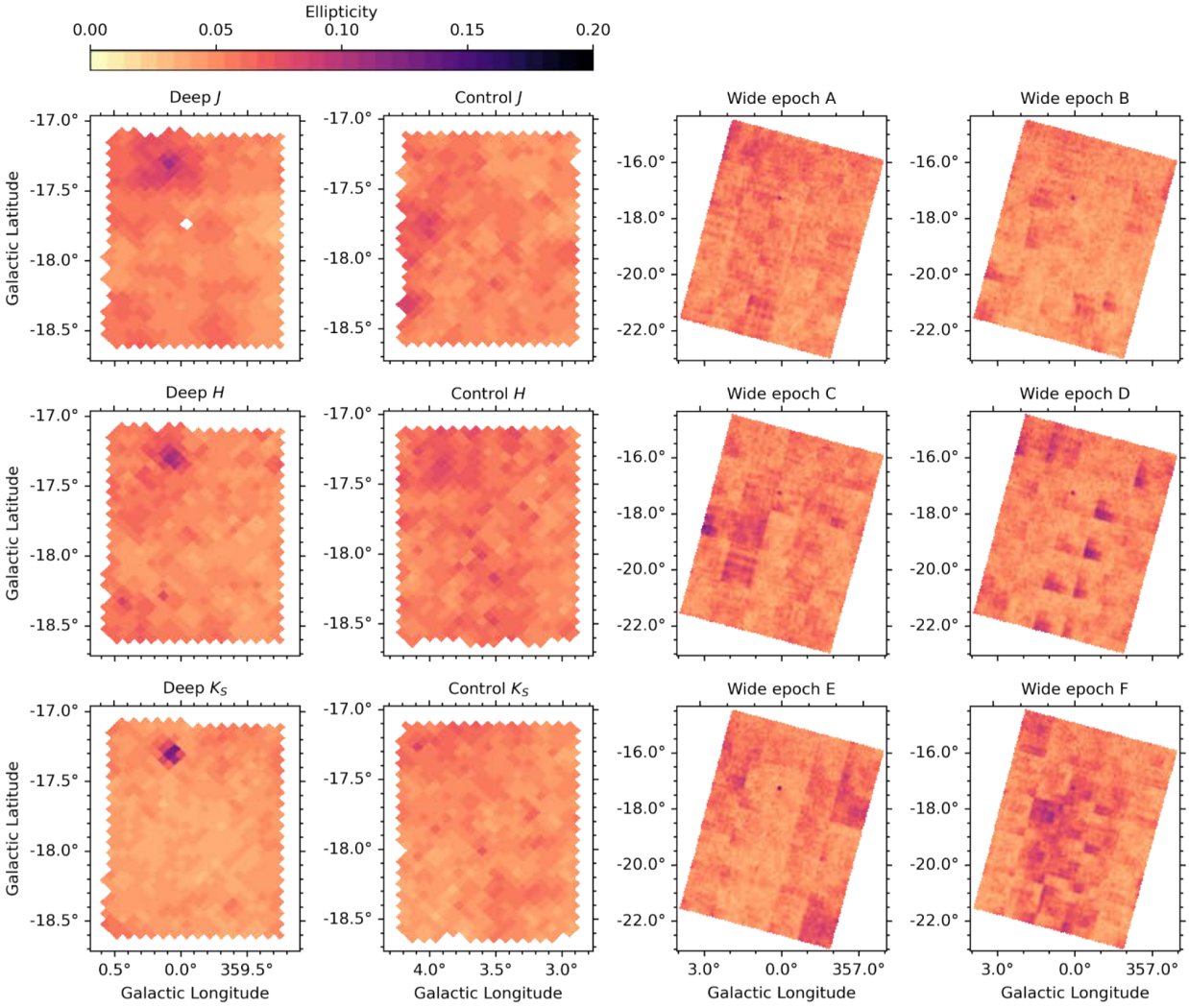


**Fig. 8.** Median point source ellipticity on a healpix grid (nside = 1024, pixel area ~ 11.8 arcmin$^2$). Most areas show excellent ellipticities of < 0.05, only a few smaller regions exhibit marginally worse values. In the *deep* and *wide* fields the globular cluster NGC 6723 is distinctly visible at about l=0 deg, b=-17.3, where the number density becomes too large for the source extraction tool to separate individual sources. Also, several patches across the *wide* fields appear to have slightly higher ellipticity values.

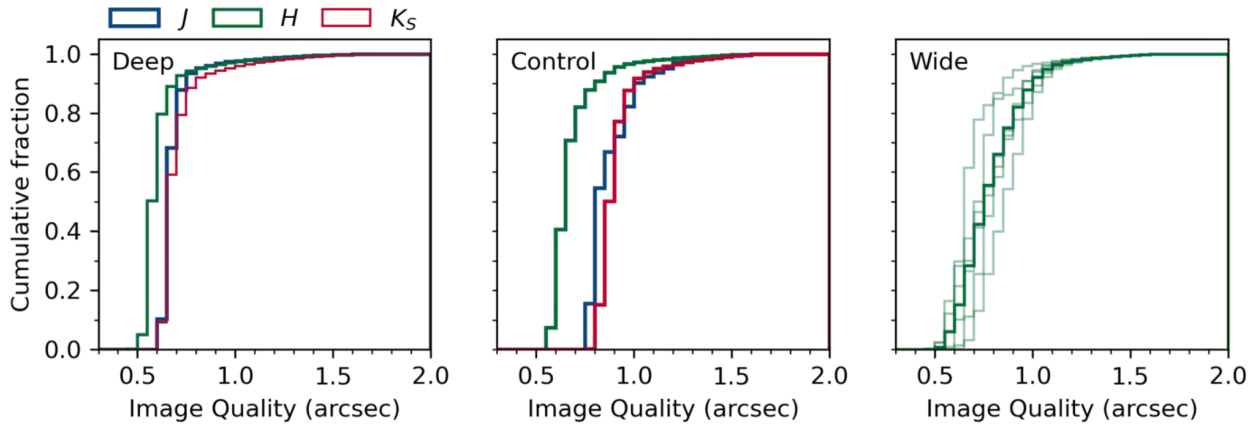


**Fig. 9.** Cumulative histograms for the measured image quality, parametrized by the point source FWHM. Most data were collected under excellent observing conditions. For the *wide* field epochs we measure a distinct spread across individual epochs.

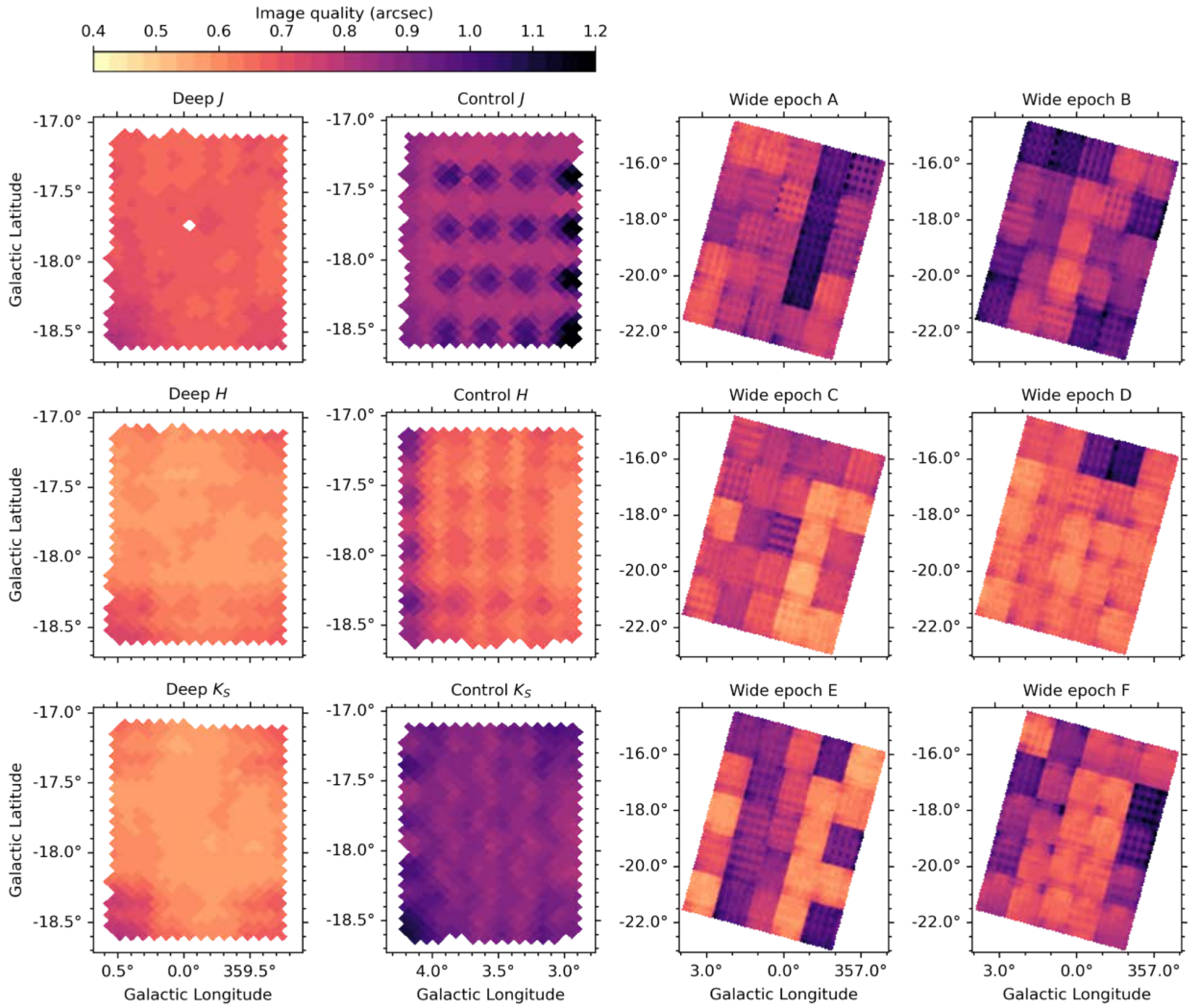


**Fig. 10.** Median image quality parametrized by the point source FWHM on a healpix grid (nside = 1024, pixel area ~ 11.8 arcmin$^2$). A typical checkerboard pattern becomes visible as a consequence of the imaging sequence with VIRCAM. Furthermore, the *wide* fields oftentimes exhibit a large degree of variation in FWHM, even on small spatial scales.

## Photometry

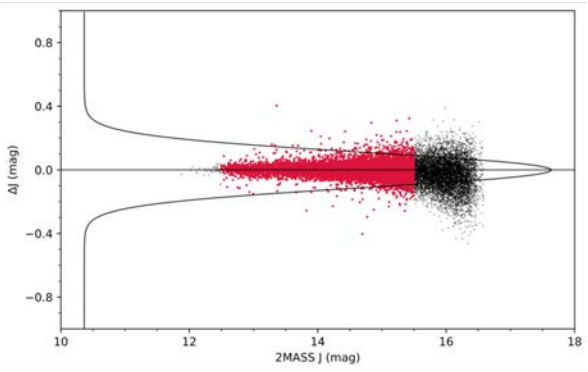


**Fig. 11.** Difference between 2MASS and VISIONS photometry as a function of 2MASS source magnitude for the Corona Australis control field in the J passband. Red points mark sources that were used for the photometric calibration, while black sources were not used due to either saturation issues or not meeting 2MASS quality criteria. The horizontal line marks the desired value of 0 mag difference between the data. The solid line is a vertical histogram of all values.

Source detection and extraction was performed with Sextractor with a detection threshold of 1.5 sigma above the local background value, while requiring a minimum of three significant pixels for a detected source. The choice of this detection threshold was already evaluated in Meingast et al. 2016 and our tests showed that this choice also yields excellent results for VISIONS data where simultaneously very faint sources are detected while keeping the contamination at a minimal level. Magnitudes and magnitude errors were also calculated by Sextractor. The photometric calibration was performed by comparing the measured magnitudes to published 2MASS fluxes. Here, only sources with quality flat A or B in 2MASS were used in addition to a hard-coded magnitude limit at the bright end to avoid contamination by sources close to the detector saturation levels. Figure 11 shows the comparison of VISIONS photometry to 2MASS for the *control* field in the J band. In this figure, red points display sources that were used for the photometric calibration. The scatter observed in this diagram is mostly caused by statistical errors from the 2MASS catalog. The typical error level of the determined zero-points (computed as the standard error of the mean) is below 1%.

Figure 12 shows a comparison of 2MASS and VISIONS photometry for all sub-surveys. The figure reveals no prominent systematic pattern, hinting at a mostly bias-free photometric calibration across all data products. Only the panels for the *wide* fields in the two columns on the right-hand side show a low-amplitude pattern reminiscent of the tile coverage in Fig. 1.

Sensitivity limits for the survey were estimated with the S/N value supplied by Sextractor (not included in the source catalogs). Figures 13 shows the 5-sigma sensitivity limits in both the form of histograms (top panel) and again mapped onto a healpix grid (bottom panel), respectively. For the *control* field, we find the faintest sensitivity limits for all passbands, with a median values of 21.8 mag, 21.1 mag, and 19.9 mag in J, H, Ks, respectively. The limits for the *deep* fields are brighter because the observations were split into two OBs: 21.5 mag in J, 20.8 mag in H, and 19.4 mag in Ks. For the *wide* field, the H-band median sensitivity limit is 19.8 mag.

Finally, as a measure of photometric reliability, we plot the color-magnitude and color-color diagrams for the deep and control fields in Figs. 14 and 15. Especially the color-color diagram of the deep field reveals the characteristic scattering of sources along the extinction vector.

This data release contains different kinds of measurements for source magnitudes:

- ➔ A total of 16 fixed circular apertures in the source catalog column MAG_APER: 3.0, 4.0, 5.0, 6.0, 7.0, 8.0, 9.0, 10.0, 12.0, 14.0, 16.0, 18.0, 21.0, 24.0, 27.0, and 30.0 pix. Thus, at a pixel scale of ⅓ arcsec/pix, the diameters range from 1 arcsec to 10 arcsec. Aperture matching was performed for all diameters where the aperture correction was calculated relative to the largest aperture. When working with these fixed apertures, we recommend using the 2 arcsec aperture, which represents a balance between capturing a significant amount of the PSF flux and the S/N. For each of these apertures, the catalogs include a corresponding error in the column MAGERR_APER.
- ➔ In addition to the fixed aperture magnitudes, we also include automatic measurements from Sextractor (details are available in the Sextractor user manual[1]). We recommend using these values when working with VISIONS photometry.

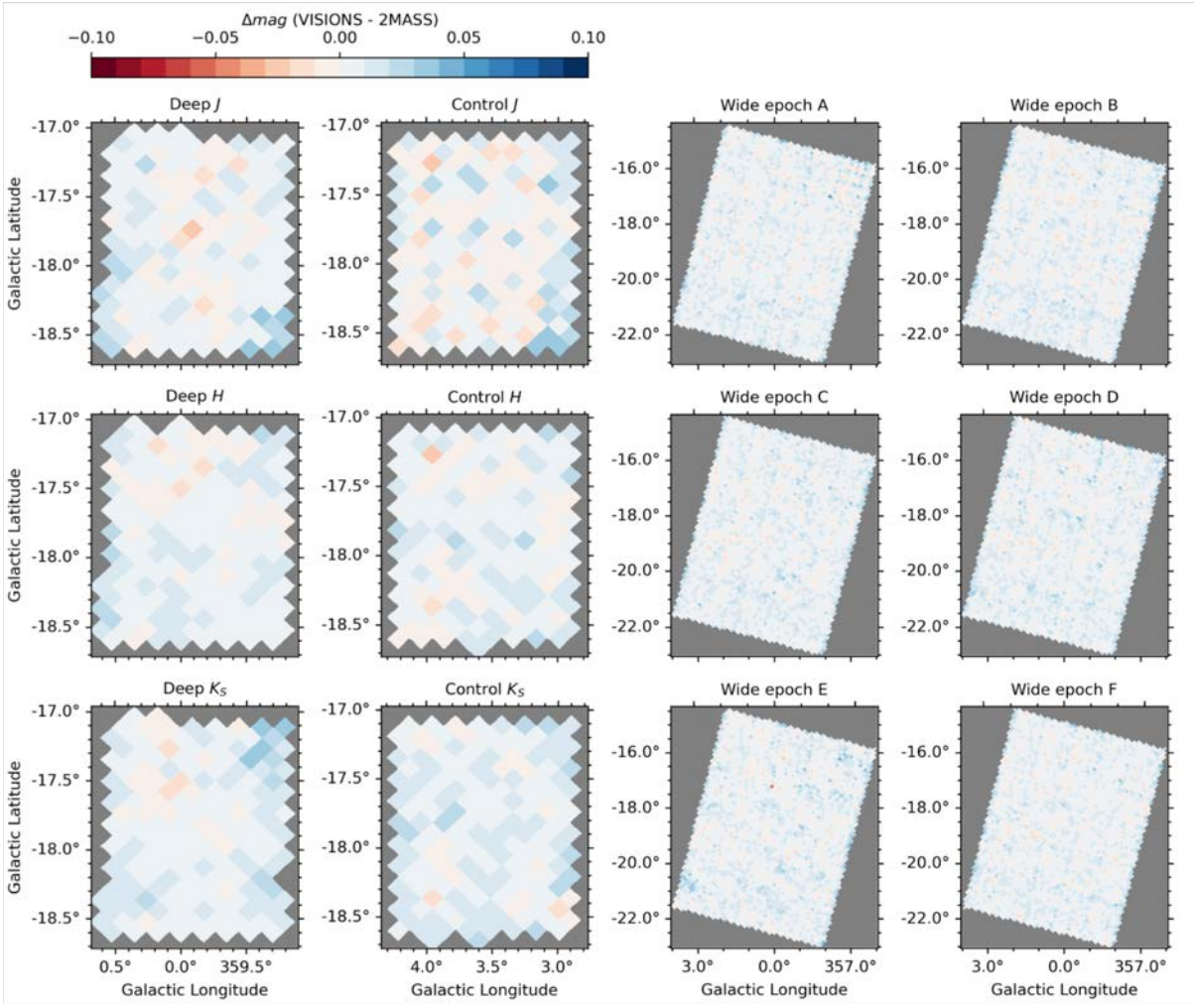


**Fig. 12.** Comparison of 2MASS and VISIONS photometry mapped onto a healpix grid (nside = 512, pixel area ~ 47.2 arcmin$^2$). The overall photometric calibration for this data release appears to be largely free from systematic differences across the fields. Only for the *wide* fields there appears to be a minor residual pattern at the percent-level.

[1] https://sextractor.readthedocs.io/en/latest/

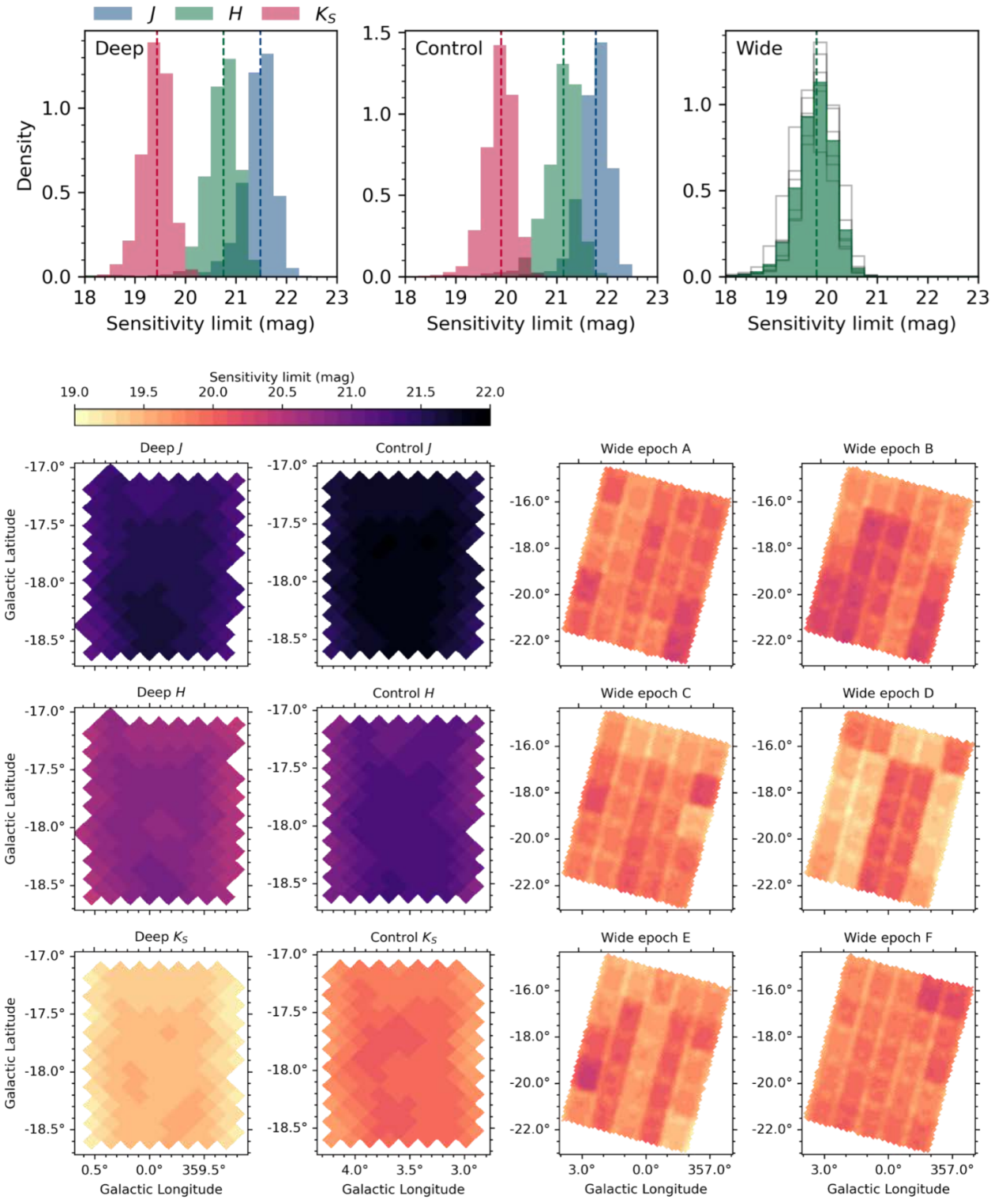


**Fig. 13.** Top: Sensitivity limit (5 sigma) histograms for all sub-surveys. Bottom: Sensitivity limits mapped onto a healpix grid (nside = 512, pixel area ~ 47.2 arcmin$^2$). While the *deep* and *control* data show rather uniform sensitiviy across the field, for the *wide* data we find again a pattern related to different observing conditions.

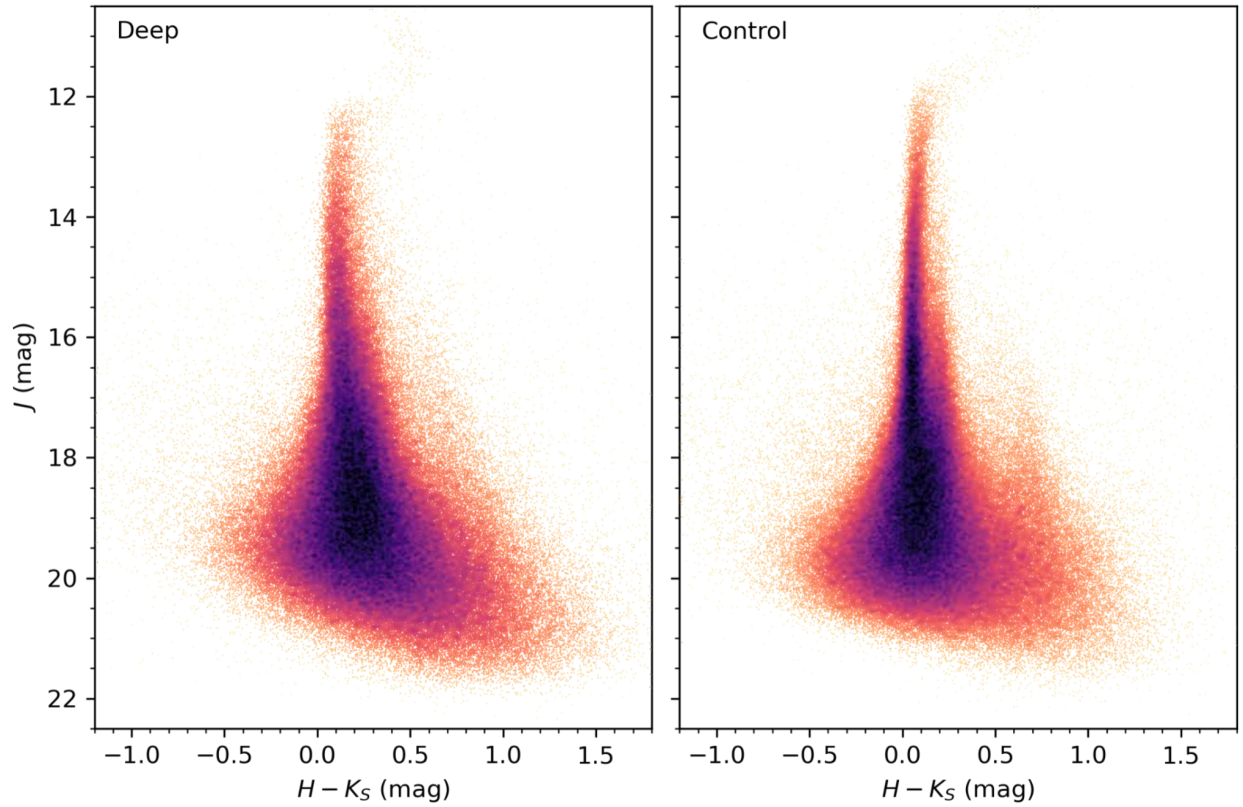


**Fig. 14.** Color-magnitude diagram for the *deep* (left panel) and *control* field (right panel). A comparison of the diagrams clearly shows the broader sequence extending to red colors for the *deep* field due to extinction from the molecular cloud.

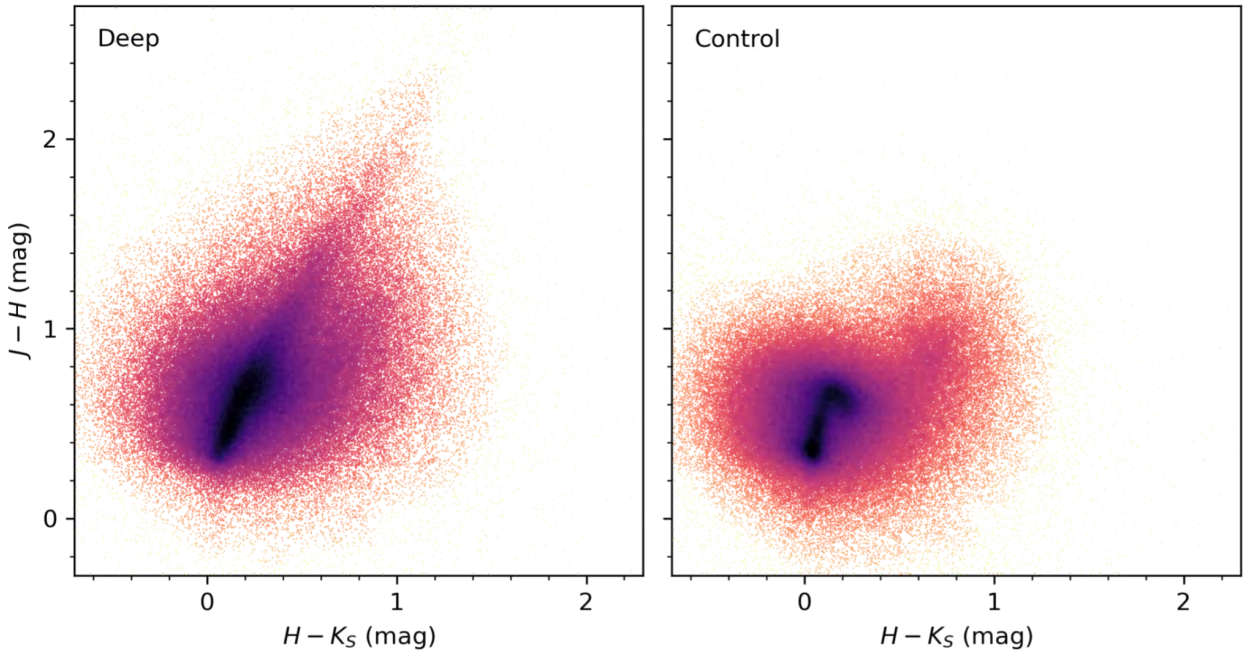


**Fig. 15.** Color-color diagram for the *deep* (left) and *control* fields (right). The *control* field shows a well defined main sequence with the typical bend for late spectral type sources at about (H - Ks) ~ 0.2 mag, (J - H) ~ 0.7 mag. The *deep* field shows the characteristic scattering of sources along the extinction vector.

## Astrometry

The astrometric calibration of the data was performed with Scamp, using Gaia EDR3 as the reference catalog[2]. Non-linear geometric distortions were fitted using a fourth order polynomial. The average reported astrometric dispersion (rms) with respect to Gaia amounts to 17.9 mas, while the average internal dispersion (i.e. comparing source positions as measured on the images) amounts to 18.4 mas. The similarity of these values shows that the astrometric accuracy is limited by the VISIONS data and not the reference catalog. A typical dispersion plot for the astrometric calibration is shown in Fig. 5. Figure 16 shows the astrometric dispersion mapped on a healpix grid. Only point-like sources with S/N > 50, ruwe < 1.5, and a proper motion error < 1 mas/yr were used to compute the 1-sigma dispersion in positional differences

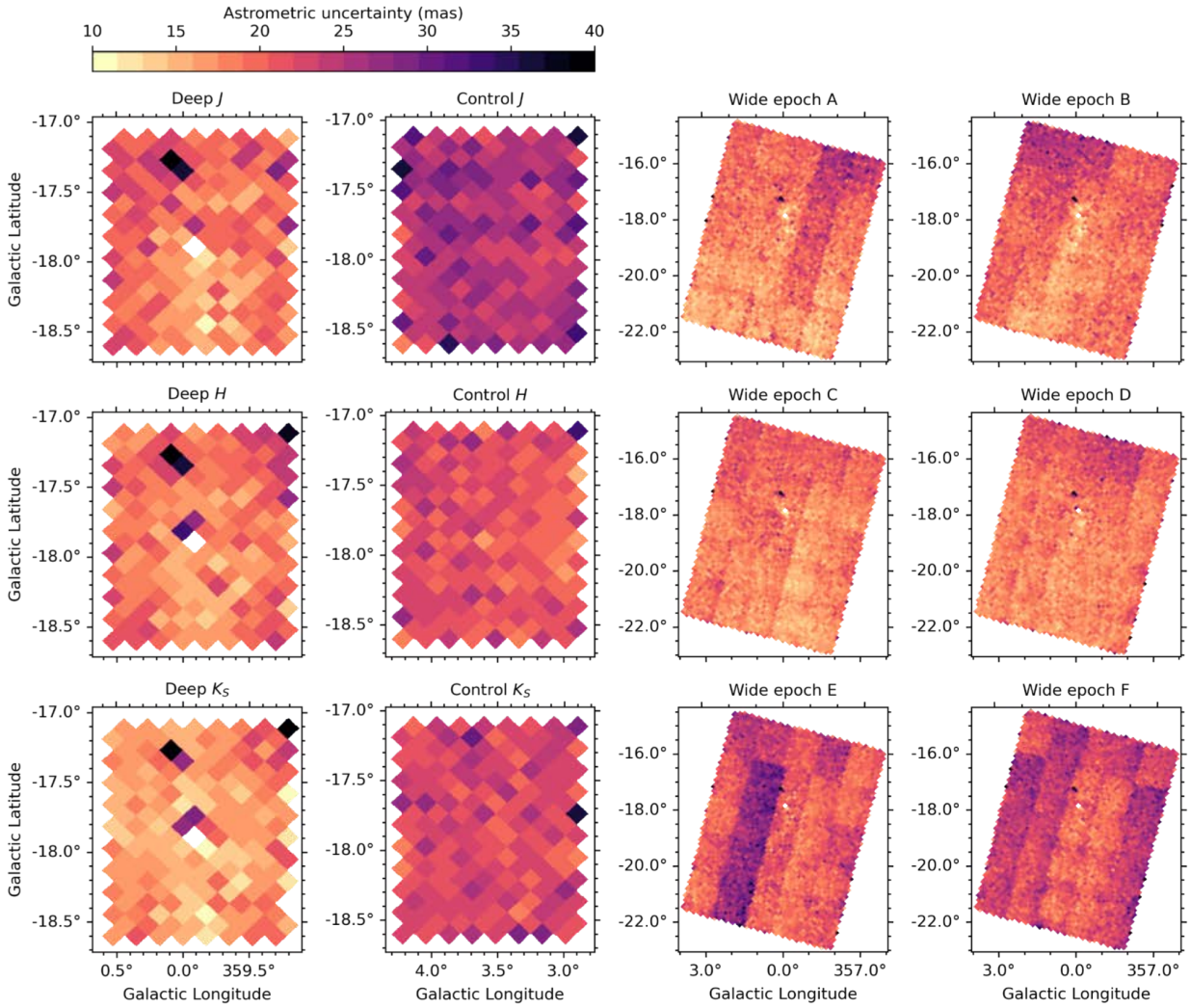


**Fig. 16.** Astrometric uncertainty mapped onto a healpix grid (nside = 512, pixel area ~ 47.2 arcmin$^2$). The *deep* and *control* fields appear uniform, while the *wide* data again shows a characteristic pattern related to the tiling of the field.

[2] Despite Gaia being an optical survey, the calibration also produced very reliable results in regions with large amounts of extinction.

between VISIONS sources and Gaia EDR3. Similar to the values reported by Scamp, this metric also shows a dispersion on the order of 20 mas, with several significant differences on local scales. A comparison to Fig. 10. reveals a correlation with image quality, i.e. larger astrometric uncertainty for fields with worse image quality.

## Data Format

### File types and naming convention

This release contains image data and source catalogs. Generally, the image data are provided in two different types, depending on the data product:

- Fully contiguous tiles are stored as FITS images with only one primary header-data-unit; no extensions are present in these files. The filenames for tiles end with *tl.fits*.
- Stacked pawprints are also stored in FITS format, but contain a primary header-data-unit and 16 extensions, each representing a VIRCAM detector. The filenames for these stacks end with *st_[01-06].fits* where the numbers refer to each individual offset position.

Each image file is associated with a weight map, with the filename ending with *weight.fits* and corresponding source tables, with the filename ending with *sources.fits*. Source tables and weight maps are also provided in the FITS format.

The overall naming convention for all data products is best explained with an example. For instance, the first observed *deep* tile in the J passband is named CrA_deep_J_1_tl.fits. The corresponding weight map and source catalog would then be CrA_deep_J_1_tl.weight.fits and CrA_deep_J_1_tl.sources.fits, respectively. For *control* observations, the filenames contain *control* instead of *deep*. For the *wide* data, the name contains the string *wide* and references also the corresponding epoch. Furthermore, the *wide* file names also include the position of a tile in the 5x5 mosaic (see Fig. 1). For example, the stacked pawprint of the fifth offset during the OB execution of the central tile in the 5x5 pattern of the *wide* sub-survey in epoch C is named CrA_wide_1_3_3_C_st_05.fits. The first number in the filename refers to the global field number within the observing region. For Corona Asutralis, VISIONS contains only one such region, hence this number is always 1.

## Source catalog columns

The following list contains a description of each column in the tables provided with this data release. When using photometry from this data release, we recommend the automatic Sextractor magnitude and applying quality criteria with the Sextractor flag and restricting the FWHM to sensible values. The epoch for the coordinates corresponds to the observing time of each data product (found in the corresponding FITS header). For most applications, however, a mean epoch of 2018.5 can be assumed.

| **Column name** | **Description** | **Unit** |
|---|---|---|
| RA | Source right ascension | deg |
| DEC | Source declination | deg |
| ERRMAJ | Semi-major axis of position error ellipse | mas |
| ERRMIN | Semi-minor axis of position error ellipse | mas |
| ERRPA | Position angle of error ellipse major axis E of N | deg |
| MAG_APER | Fixed aperture magnitudes for 16 diameters from 1 to 10 arcsec | mag |
| MAGERR_APER | Errors for fixed aperture magnitudes | mag |
| MAG_AUTO | Automatic magnitude | mag |
| MAGERR_AUTO | Error for automatic magnitude | mag |
| FWHM | Source full width at half maximum | arcsec |
| ELLIPTICITY | Source ellipticity | |
| SFLG | Sextractor extraction flag | |

## Acknowledgments

Based on data products created from observations collected at the European Organization for Astronomical Research in the Southern Hemisphere under ESO programme(s) 198.C-2009

This research has made use of the services of the ESO Science Archive Facility.

This work has made use of data from the European Space Agency (ESA) mission Gaia (https://www.cosmos.esa.int/gaia), processed by the Gaia Data Processing and Analysis Consortium (DPAC, https://www.cosmos.esa.int/web/gaia/dpac/consortium). Funding for the DPAC has been provided by national institutions, in particular the institutions participating in the Gaia Multilateral Agreement.

## References

Automatic Astrometric and Photometric Calibration with SCAMP, E. Bertin, 2006, ADASS XV, Vol. 351, p.112
First Scientific Results from the VISTA Hemisphere Survey (VHS), R. G. McMahon et al., The Messenger, 154, 35-37
Gaia Early Data Release 3. Summary of the contents and survey properties, Gaia Collaboration, 2021, A&A, 649, A1
SExtractor: Software for source extraction, Bertin & Arnouts, 1996, A&AS, 117, 393
SWarp: Resampling and Co-adding FITS Images Together, Bertin, 2010, ASCL, ascl:1010.068.
The Two Micron All Sky Survey (2MASS), M. F. Skrutskie et al.2006, AJ, 131, 1163-1183
The Gaia mission, Gaia Collaboration, 2016, A&A, 595, A1
VISION - Vienna survey in Orion. I. VISTA Orion A Survey, S. Meingast et al., 2016, A&A, 587, A153